Title

Ionization-assisted spatiotemporal localization in gas-filled capillaries.

Journal

Optics Letters, 43(13)

ISSN

0146-9592

Authors

Gao, Xiaohui

Patwardhan, Gauri

Shim, Bonggu

et al.

Publication Date

2018-07-01

DOI

10.1364/ol.43.003112

Peer reviewed

Optics Letters

Ionization-assisted spatiotemporal localization in gas-filled capillaries

Xiaohui Gao,[1] Gauri Patwardhan,[1,2] Bonggu Shim,[3] Tenio Popmintchev,[4,5] Henry C. Kapteyn,[6] Margaret M. Murnane,[6] and Alexander L. Gaeta[1,*]

[1]Applied Physics and Applied Mathematics Department, Columbia University, New York, New York 10027, USA
[2]School of Applied and Engineering Physics, Cornell University, Ithaca, New York 14853, USA
[3]Department of Physics, Applied Physics and Astronomy, Binghamton University, Binghamton, New York 13902, USA
[4]Department of Physics and Center for Advanced Nanoscience, University of California San Diego, La Jolla, California 92093, USA
[5]Photonics Institute, TU Wien, Gusshausstrasse 27-387, A-1040 Vienna, Austria
[6]JILA, University of Colorado, Boulder, Colorado 80309, USA
*Corresponding author: a.gaeta@columbia.edu

Received 18 April 2018; revised 26 May 2018; accepted 30 May 2018; posted 31 May 2018 (Doc. ID 328140); published 25 June 2018

We demonstrate numerically and experimentally that intense pulses propagating in gas-filled capillaries can undergo localization in space and time due to strong plasma defocusing. This phenomenon can occur below or above the self-focusing threshold P_{cr} as a result of ionization-induced refraction that excites higher-order modes. The constructive interference of higher-order modes leads to spatiotemporal localization and resurgence of the intensity. Simulations show that this confinement is more prominent at shorter wavelength pulses and for smaller capillary diameters. Experiments with ultraviolet pulses show evidence that this ionization-induced refocusing appears below P_{cr} and thus represents a mechanism for spatiotemporal confinement without self-focusing.

OCIS codes: (190.7110) Ultrafast nonlinear optics; (350.5500) Propagation; (260.3230) Ionization.

https://doi.org/10.1364/OL.43.003112

Propagation of intense pulses in gases is inevitably accompanied by ionization. The resulting plasma defocusing reduces the laser intensity and shortens the effective interaction length of nonlinear processes such as high-harmonic generation (HHG) and supercontinuum generation. To overcome this limit, various approaches of guiding intense pulses have been developed. Kerr-induced filamentation can be utilized under conditions of weak ionization [1]. Shock-formed plasma waveguides [2] and gas-filled capillary discharge waveguides [3] exploit the transversely decreasing refractive index and enable total internal reflection. However, this approach is restricted to a narrow range of plasma densities. Pulses can also be guided using glancing incidence reflection in capillaries [4] or antiresonant reflection in photonic crystal fibers [5]. In hollow fibers, monomode guiding of the fundamental mode is preferred owing to its small attenuation and has been demonstrated when the plasma density is low [6]. As the laser intensity increases, strong nonlinear interactions excite higher-order modes in waveguides, and the spatiotemporal coupling of these modes gives rise to new phenomena such as pulse self-compression [7] and generation of multimode optical solitons [8].

Recent experiments have demonstrated efficient generation of high-order harmonics beyond the water window driven by UV pulses in a capillary filled with gases near atmospheric pressures, which must be occurring in multiply-ionized plasmas [9]. The HHG emission is optimized at a capillary length of 1.3 cm and gas pressure of several hundred torr. Normally, the coherence length of phase matching in such highly ionized plasma is only 1.5 μm, and the absorption length is 1.3 mm, if the linear and nonlinear indices of the ions are not taken into account. Moreover, efficient soft x-ray harmonic generation suggests that a laser intensity of 6×10^{15} W/cm^2 is sustained over some length in the capillary waveguide, that is, some form of spatiotemporal localization occurs.

In this Letter, we show through simulations that such spatiotemporal localization can occur through the combined effect of plasma defocusing and reflection from the capillary walls and is unrelated to P/P_{cr}. We also show that at higher powers $P \gg P_{cr}$ this localization can be enhanced, in contrast to the common belief that self-focusing limits the pulse energy for ionization-induced pulse compression and high powers should be avoided [10,11]. Simulations indicate that spatiotemporal localization is enhanced by using smaller capillary radii and shorter wavelengths, and since plasma generation depends on the laser intensity, focusing more tightly into the waveguide core is beneficial for excitation of higher-order modes and inducing strong spatiotemporal nonlinear localization. Our experiments with ultraviolet pulses provide evidence that refocusing reminiscent of self-focusing occurs for $P < P_{cr}$.

We model nonlinear propagation in a gas-filled capillary using the nonlinear envelope equation [12] with a modal expansion [13,14] for the transverse coordinates. For a linearly polarized beam with cylindrical symmetry, the electric field can be approximated as

$$E(r,t,z)=\sum_n \mathcal{E}_n(t,z)J_0(k_{\perp,n}r)\exp(ik_{z,0}z-i\omega_0 t), \quad (1)$$

where $\mathcal{E}_n(t,z)$ is the complex modal envelope; $J_0(k_{\perp,n}r)$ is the zeroth-order Bessel function; n is the mode index; $k_{\perp,n}=u_n/a$ is the axial wave number with u_n the nth root of the equation $J_0(u_n)=0$; a is the radius of the capillary; and $k_{z,n}$ is the wave number in the propagation direction:

$$k_{z,n}(\omega,k_{\perp,n})=\sqrt{k^2(\omega)-k_{\perp,n}^2}, \quad (2)$$

where $k(\omega)=\omega n(\omega)/c$, ω is angular frequency, $n(\omega)$ is the refractive index, and c is the speed of light. The evolution of each modal component is described by [15]

$$\frac{\partial\tilde{\mathcal{E}}_n}{\partial\zeta}=i[k_{z,n}(\omega)+i\alpha_n-\kappa(\omega)]\tilde{\mathcal{E}}_n+\frac{i}{2k_{z,n}}\frac{\omega^2}{\epsilon_0c^2}\left(\tilde{P}_{\mathrm{NL},n}+i\frac{\tilde{\mathcal{J}}_n}{\omega}\right), \quad (3)$$

where $\sim$ indicates that the quantity is in the frequency domain, ζ is the propagation distance, $\kappa(\omega)=k_0+(\omega-\omega_0)/v_g$, and v_g is the group velocity of the fundamental mode. Under the condition $k_0a\gg u_n$, the loss coefficient α_n is given by [16], $\alpha_n=\frac{1}{2}\left(\frac{u_n}{2\pi}\right)^2\frac{\lambda^2}{a^3}\frac{1+\epsilon_{\mathrm{cl}}}{\sqrt{\epsilon_{\mathrm{cl}}-1}}$, where ϵ_{cl} is the dielectric constant of the cladding. Kerr-nonlinearity and ionization effects are included in $\tilde{P}_{\mathrm{NL}}$ and $\tilde{\mathcal{J}}$, which are calculated in the frequency domain using the following expressions:

$$\tilde{P}_{\mathrm{NL}}=2\epsilon_0n_0\widetilde{n_2\mathcal{I}\mathcal{E}}, \quad (4)$$

$$\tilde{\mathcal{J}}=-\frac{n\omega}{2k_{z,n}c}\frac{\sum_i W_iU_{\mathrm{pi}}\widetilde{\rho_i\mathcal{E}}}{\mathcal{I}}+\frac{e^2}{m_e}\frac{\tau_c}{1-i\omega\tau_c}\widetilde{\rho\mathcal{E}}, \quad (5)$$

where n_2 is the nonlinear refractive index; $\mathcal{I}$ is the laser intensity; $\tilde{\mathcal{E}}=\sum_n\tilde{\mathcal{E}}_nJ_0(k_{\perp,n}r)$; W_i is the ionization rate [17]; ρ_i and U_{pi} are the density and ionization potential of ions of ith charge state, respectively; e and m_e are the electron charge and mass, respectively; τ_c is the collision time between the electrons and ions or neutral atoms; and ρ is the electron density. The number density ρ_i is calculated from the rate equations. The terms $\tilde{P}_{\mathrm{NL}}$ and $\tilde{\mathcal{J}}$ lead to mode coupling, and their modal components $\tilde{P}_{\mathrm{NL},n}$ and $\tilde{\mathcal{J}}_n$ are substituted into Eq. (3). An alternative approach without modal decomposition can be found in [18].

While simulations near atmospheric pressure and above using the nonlinear envelope equation predict femtosecond filamentation in free space, the laser intensity remains moderate owing to intensity clamping [19]. For simulations of pulse propagation in gas-filled hollow fibers, the intensity is typically near or just above the ionization threshold [11,20]. In our simulations, the intensity is as high as 6×10^{15} W/cm^2, producing multiply-ionized plasmas. Therefore, we include multiple ionization up to Ar^{7+}. The nonlinear refractive index due to the depletion of neutral atoms and generation of ions is calculated using $n_2=\sum n_{2,i}\rho_i/\rho_0$ with $n_{2,i}$ given by Table S2 in Ref. [9]. The effect of τ_c is negligible, and we assume electron-ion collision time is the same as that of electron-neutral collision in calculating τ_c. The number of modes in the simulation is selected carefully to ensure the convergence of the results as mode number increases.

Figure 1 shows the simulation results for a 2-mJ, 35-fs, 270-nm pulse propagating in a capillary filled with 200-torr argon gas ($P/P_{\mathrm{cr}}=27$, Keldysh parameter $\gamma=0.439$ for ionizing Ar), similar to the conditions in [9]. The capillary is composed of three sections with a total length of 1.3 cm and density gradient at each end [9]. The spatiotemporal profiles at the entrance ($z=0$), defocusing region ($z=0.36$ cm), and refocusing region ($z=1.0$ cm) are shown in Fig. 1(a). The input beam size $w=0.23a$ is much smaller than that for optimal coupling into the fundamental mode ($w=0.65a$). Loss at the higher-order modes is insignificant for this length, and tight focusing at the input allows a high input intensity of 6×10^{15} W/cm^2. The defocused beam is reflected by the capillary wall and interferes with the undeflected portion of the beam, producing the fringes in the second profile. The evolution of the on-axis peak intensity during the propagation is plotted in Fig. 1(b). A defocusing region and a refocusing region are identified. It is important that a high intensity occurs inside the capillary. Due to the gas-vacuum interface, the gas pressure reaches maximum inside the capillary, where the pulse can interact with the high gas density. Figure 1(c) shows the fluence distribution along the capillary in which a narrow string appears in the refocusing region. Figure 1(d) is the on-axis temporal profile. Since the defocused beam undergoes a large angle reflection, it is composed by higher-order modes with group velocities slower than that of the fundamental mode. The pulse duration is shorter than the input since the spectrum is broadened and the group-velocity dispersion of higher-order modes $\partial^2k_z/\partial^2\omega$ is anomalous, which results in pulse compression. Figure 1(e) shows the integrated spectrum along the propagation distance, and a strong blueshift occurs, which is primarily caused by the ionization.

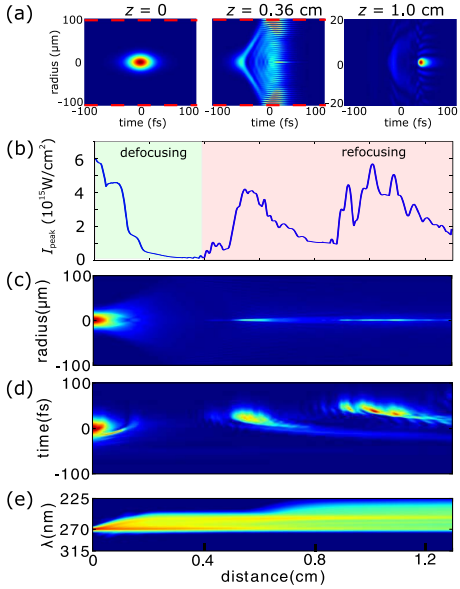

Fig. 1. Numerical simulation of a 35-fs pulse at 270 nm propagating in a 200-torr Ar gas-filled capillary of 200-μm diameter. (a) Spatiotemporal profiles at $z=0$, 0.36, and 1.0 cm. The horizontal dashed line indicates the capillary dimension. (b) On-axis peak intensity as a function of the propagation distance. The light green and light red sections indicate the defocusing and refocusing regions. (c) Fluence distribution as a function of the propagation distance. (d) On-axis temporal profile versus propagation distance. (e) Integrated spectrum (log scale) versus propagation distance.

This recovery of the intensity appears similar to that in femtosecond filamentation caused by dynamic spatial replenishment [21], in which the intensity peaks again when the tail of the defocused pulse refocuses due to self-focusing. To investigate the role of self-focusing, we artificially include or remove the n_2 of the atoms and ions, and the resulting on-axis peak intensity and on-axis fluence are shown in Figs. 2(a) and 2(b), respectively, for $P = 50$ GW. We show the following three cases: n_2 of atoms and ions is included (solid blue curve), n_2 of ions is set to zero (dashed green curve), and n_2 of atoms and ions are both set to zero (dotted red curve). Thus the solid blue curve corresponds to $P/P_{cr} = 27$, and the dotted red curve represents $P < P_{cr} = \infty$. The dashed green curve nearly overlaps with the solid blue curve, indicating that n_2 of ions plays little role in the propagation dynamics, although it is essential for achieving effective phase-matching in high-harmonic generation [9]. The refocusing pattern is similar for all three curves, indicating that self-focusing does not play a role in the spatial confinement mechanism. Note that the fluence rises to half of the input while the intensity increases to almost that of the input, which is due to pulse self-compression during propagation. In the refocusing region, switching on n_2 increases the maximum peak intensity by 16% because n_2 affects the pulse in the time domain through spectral broadening via self-phase modulation.

Simulations for input energies of 1 and 0.02 mJ are shown in Fig. 3(a), which illustrate this ionization-assisted confinement. The capillary length is 6 cm. For $E_{in} = 0.02$ mJ, the pulse undergoes linear propagation and the intensity drops monotonically over several centimeters. As the energy is increased to 1 mJ, substantial ionization occurs, which defocuses the beam within a half centimeter, and a narrow filament string follows. The appearance of this confinement depends on the intensity only; thus a tighter input focusing is beneficial. The intense pulse produces a plasma, which defocuses the beam. After reflection on the capillary wall, the diverging beam converges back to the center of the capillary. However, it does not converge to a single point. The smaller the divergence angle of the defocused beam, the greater the distance at which it will be refocused. Due to the spread of divergence angles, the refocusing takes place for a certain length and forms a long filament. Moreover, additional plasma is produced at the position of the intensity spikes, resulting in further defocusing. Equivalently, this confinement can be described as the constructive interference of higher-order modes excited by plasma defocusing.

Gas density also plays an important role in this confinement phenomenon. The intensity evolution at different pressures is shown in Fig. 3(b). For lower pressures, it requires a longer distance to refocus. However, if the pressure is too high, ionization loss becomes significant. The optimal pressure is found to be several hundred torr, which is close to that used in the experiments for optimal high-harmonic generation [9].

The dependence of the confinement on wavelength and capillary size is shown in Fig. 4. In the simulations of Figs. 4(a) and 4(b), 50-fs, 0.15-mJ pulses with $\lambda =$ 270 nm, 800 nm, or 2.0 μm are propagating in a 155-μm diameter capillary filled with 1-atm argon gas. Simulations using three capillary sizes for 800-nm pulses are shown in Figs. 4(c) and 4(d). The confinement is favored at UV wavelengths and small capillary sizes. The coherence length of different modes can be defined as $\pi/|k_{z,m} - k_{z,n}| \propto 1/\lambda$, where m and n are the mode order. Thus, at shorter wavelength, constructive interference with more modes can be maintained for a longer distance, as shown in Fig. 4(a). For smaller capillaries, higher-order modes are excited more efficiently. As the capillary size increases, the confinement gets weaker and eventually converges to the free space behavior.

We observe evidence of this ionization-induced refocusing experimentally when 400-nm, 40-fs pulses are tightly focused into a 2-cm capillary of 155-μm inner diameter in air using a lens with $f = 10$ cm. The profile at the linear focus is shown in Fig. 5(a). The beam profile at the exit of the capillary is imaged. We choose the linear focus to be approximately 2 mm into the capillary to ensure all the light is collected by the capillary when ionization occurs. The profile for linear propagation ($E_{in} = 2.8$ μJ) is a ring structure as shown in Fig. 5(b), which

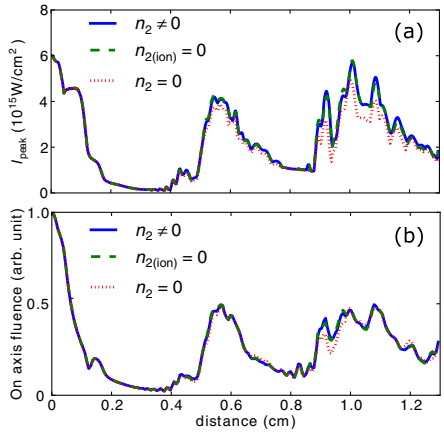

Fig. 2. On-axis (a) peak intensity and (b) fluence during propagation for the following three simulation conditions: (i) n_2 of neutral atoms and ions are included (solid blue curve); (ii) n_2 of ions is not included (dashed green curve); (iii) n_2 of neutral atoms and ions are set to zero (dotted red curve).

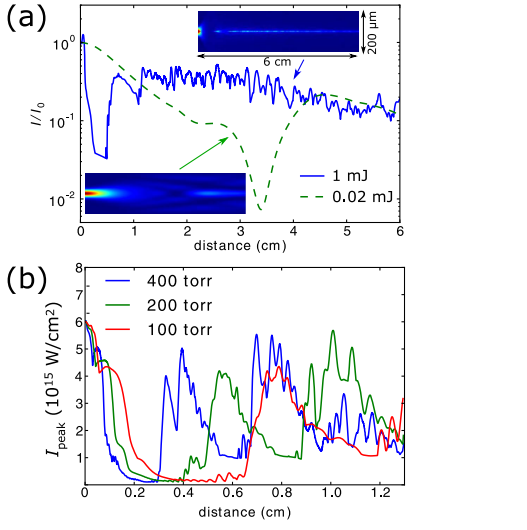

Fig. 3. (a) On-axis peak intensity as a function of the propagation distance for $E_{in} = 0.02$ mJ and 1 mJ. The inserts are the fluence distribution along the propagation distance for the two curves. (b) On-axis peak intensity as a function of the propagation distance for different pressures.

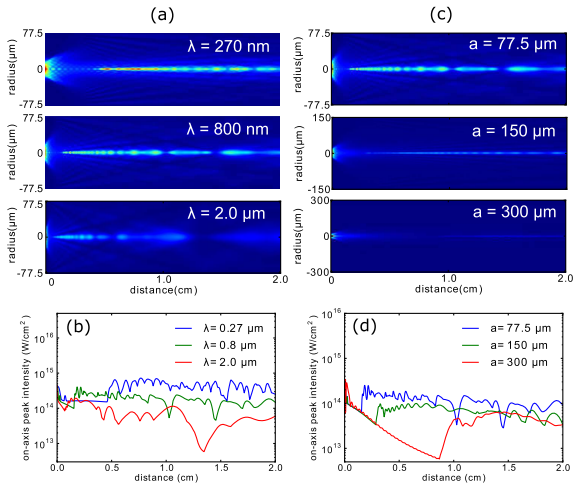

Fig. 4. (a) Fluence distribution along the propagation distance for three wavelengths: $\lambda = 270$ nm, 800 nm, and 2.0 μm. (b) On-axis peak intensity as a function of the propagation distance for three wavelengths. (c) Fluence distribution along the propagation distance for three capillary radii: $a = 77.5$, 150, and 300 μm. (d) On-axis peak intensity as a function of the propagation distance for three capillary radii.

is due to destructive interference of different modes on axis. For $E_{\text{in}} = 45$ μJ, a peak with narrow width is observed. The input power is approximately equal to $0.5P_{\text{cr}}$, ionization is confirmed from the fluorescence, and the Keldysh parameter γ is 0.63. Figure 5(d) shows the lineout of the profiles of Figs. 5(a) and 5(c). Figure 5(e) shows full-width at half-maximum (FWHM) sizes of consecutive shots at the exit of the capillary and in free space. While the FWHM sizes are 8.75 ± 0.24 μm (V) and 9.08 ± 0.29 μm (H) in free space, they shrink to 7.26 ± 0.76 μm (V) and 8.49 ± 2.57 μm (H) with the capillary. Due to the pointing stability of the incoming laser pulse, some shots have imperfect alignment, resulting in larger size in particular in the horizontal direction. For the majority of the

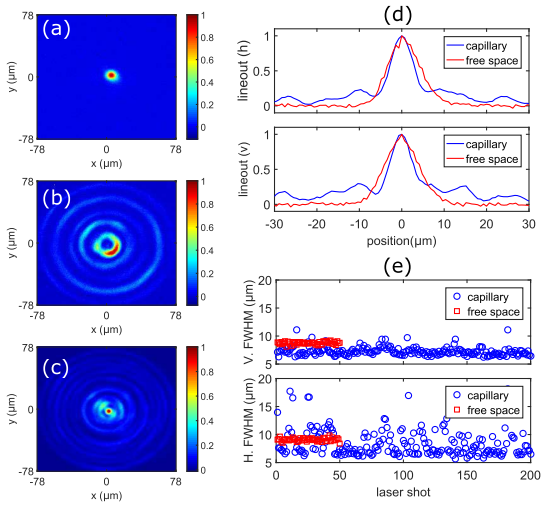

Fig. 5. (a) Beam profile at the focus in free space. (b) Beam profile at the capillary exit for $E_{\text{in}} = 2.8$ μJ. (c) Beam profile at the capillary exit for $E_{\text{in}} = 45$ μJ. (d) Horizontal and vertical lineout of beam profile at the capillary exit and in free space. (e) FWHM sizes for a series of consecutive shots at the capillary exit and in free space.

shots, we observe a reduction in size in both directions, which confirms the ionization-induced refocusing at $P < P_{\text{cr}}$. In particular, the measured minimum size is reduced from 8.1 μm in free space to 6.2 μm with the capillary in the vertical direction, and from 8.4 to 5.7 μm in the horizontal direction.

In conclusion, we numerically and experimentally investigated nonlinear propagation of intense ultrashort pulses in a gas-filled capillary. Our results are consistent with the spatiotemporal confinement suggested by recent experiments [9]. Plasma defocusing and subsequent reflection from capillary walls induce strong spatiotemporal nonlinear localization, and self-phase modulation due to n_2 provides additional pulse temporal compression. Refocusing similar to that which occurs with self-focusing is observed experimentally for $P < P_{\text{cr}}$. Control and optimization of this localization phenomenon has practical significance for high-field experiments such as high-harmonic generation [9] and pulse self-compression [10].

Funding. Defense Advanced Research Projects Agency (DARPA) (PULSE program); Air Force Office of Scientific Research (AFOSR) (FA9550-16-1-0121); National Science Foundation (NSF) (PHY-1707237).

REFERENCES

1. A. Braun, G. Korn, X. Liu, D. Du, J. Squier, and G. Mourou, Opt. Lett. **20**, 73 (1995).
2. C. Durfee III and H. Milchberg, Phys. Rev. Lett. **71**, 2409 (1993).
3. A. Butler, D. Spence, and S. M. Hooker, Phys. Rev. Lett. **89**, 185003 (2002).
4. A. Rundquist, C. G. Durfee III, Z. Chang, C. Herne, S. Backus, M. M. Murnane, and H. C. Kapteyn, Science **280**, 1412 (1998).
5. P. Hölzer, W. Chang, J. Travers, A. Nazarkin, J. Nold, N. Joly, M. Saleh, F. Biancalana, and P. St.J. Russell, Phys. Rev. Lett. **107**, 203901 (2011).
6. F. Dorchies, J. Marquès, B. Cros, G. Matthieussent, C. Courtois, T. Vélikoroussov, P. Audebert, J. Geindre, S. Rebibo, G. Hamoniaux, and F. Amiranoff, Phys. Rev. Lett. **82**, 4655 (1999).
7. N. L. Wagner, E. A. Gibson, T. Popmintchev, I. P. Christov, M. M. Murnane, and H. C. Kapteyn, Phys. Rev. Lett. **93**, 173902 (2004).
8. W. H. Renninger and F. W. Wise, Nat. Commun. **4**, 1719 (2013).
9. D. Popmintchev, C. Hernández-García, F. Dollar, C. Mancuso, J. A. Pérez-Hernández, M. C. Chen, A. Hankla, X. Gao, B. Shim, A. L. Gaeta, M. Tarazkar, D. A. Romanov, R. J. Levis, J. A. Gaffney, M. Foord, S. B. Libby, A. Jaron-Becker, A. Becker, L. Plaja, M. M. Murnane, H. C. Kapteyn, and T. Popmintchev, Science **350**, 1225 (2015).
10. S. A. Skobelev, A. V. Kim, and O. Willi, Phys. Rev. Lett. **108**, 123904 (2012).
11. P. N. Anderson, P. Horak, J. G. Frey, and W. S. Brocklesby, Phys. Rev. A **89**, 013819 (2014).
12. A. L. Gaeta, Phys. Rev. Lett. **84**, 3582 (2000).
13. M. Nurhuda, A. Suda, K. Midorikawa, M. Hatayama, and K. Nagasaka, J. Opt. Soc. Am. B **20**, 2002 (2003).
14. C. L. Arnold, B. Zhou, S. Akturk, S. Chen, A. Couairon, and A. Mysyrowicz, New J. Phys. **12**, 073015 (2010).
15. M. Kolesik and J. Moloney, Phys. Rev. E **70**, 036604 (2004).
16. E. A. J. Marcatili and R. A. Schmeltzer, Bell Syst. Tech. J. **43**, 1783 (1964).
17. S. V. Popruzhenko, V. D. Mur, V. S. Popov, and D. Bauer, Phys. Rev. Lett. **101**, 193003 (2008).
18. J. Andreasen and M. Kolesik, Phys. Rev. E **86**, 036706 (2012).
19. A. Becker, N. Aközbek, K. Vijayalakshmi, E. Oral, C. Bowden, and S. Chin, Appl. Phys. B **73**, 287 (2001).
20. D. Novoa, M. Cassataro, J. C. Travers, and P. St.J. Russell, Phys. Rev. Lett. **115**, 033901 (2015).
21. M. Mlejnek, E. M. Wright, and J. V. Moloney, Opt. Lett. **23**, 382 (1998).